Comparing lensing and stellar orbital models of a nearby massive strong-lens galaxy

Adriano Poci ⓘ⋆ and Russell J. Smith ⓘ

Centre for Extragalactic Astronomy, University of Durham, Stockton Road, Durham DH1 3LE, UK

ABSTRACT

Exploiting the relative proximity of the nearby strong-lens galaxy SNL-1, we present a critical comparison of the mass estimates derived from independent modelling techniques. We fit triaxial orbit-superposition dynamical models to spatially resolved stellar kinematics, and compare to the constraints derived from lens modelling of high-resolution photometry. From the dynamical model, we measure the total (dynamical) mass enclosed within a projected aperture of radius the Einstein radius to be $\log_{10}(M_{\mathrm{Ein}}/\mathrm{M_\odot}) = 11.00 \pm 0.02$, which agrees with previous measurements from lens modelling to within 5 per cent. We then explore the intrinsic (de-projected) properties of the best-fitting dynamical model. We find that SNL-1 has approximately constant, intermediate triaxiality at all radii. It is oblate like in the inner regions (around the Einstein radius) and tends towards spherical at larger radii. The stellar velocity ellipsoid gradually transforms from isotropic in the very central regions to radially biased in the outskirts. We find that SNL-1 is dynamically consistent with the broader galaxy population, as measured by the relative fraction of orbit 'temperatures' compared to the CALIFA survey. On the mass–size plane, SNL-1 occupies the most-compact edge given its mass, compared to both the MaNGA and SAMI surveys. Finally, we explore how the observed lensing configuration is affected by the orientation of the lens galaxy. We discuss the implications of such detailed models on future combined lensing and dynamical analyses.

Key words: galaxies: elliptical and lenticular, cD – galaxies: kinematics and dynamics – galaxies: stellar content – galaxies: structure.

1 INTRODUCTION

The mass of a galaxy is one of the most critical properties controlling its evolution over cosmic time. This is evidenced by the plethora of observed correlations of other galactic properties with mass (e.g. Gallazzi et al. 2005; Cortese et al. 2014; Tian et al. 2021; Barone et al. 2022). Measuring the mass, however, is notoriously difficult for a number of reasons. Transforming the observed luminosity of a galaxy into a baryonic mass is prone to systematic uncertainties relating to distances, the underlying stellar populations, and complications such as dust. Moreover, a significant portion of a galaxy's mass, the dark matter (DM), is completely invisible and therefore must be inferred from its effect on luminous matter.

Direct probes of the gravitational potential can circumvent many of these issues, and can constrain the total (gravitational) mass, irrespective of the specific combination of baryonic and DM. To this end, gravitational lensing offers a relatively assumption-independent avenue for constraining the total enclosed mass within the characteristic Einstein radius θ_{Ein} (e.g. Chae 2003; Treu 2010). Moreover, in general, the confidence with which a lensing model can be constrained is dependent on the geometry and multiplicity of the images produced (e.g. Shu et al. 2015; Smith, Lucey & Collier 2018). Finally, the main degeneracy in lensing models – in particular those with only two lensed images and/or little spatial structure in the

images – is between the mass which is responsible for the lensing, and contributions from external effects (e.g. the degeneracy between mass and shear). However with high-quality data, this degeneracy can in principle be overcome by using the flux information in the pixels of the source images, rather than just their positions around the lens (Collier, Smith & Lucey 2018). Unfortunately, lensing analyses are naturally limited to the small samples of galaxies that are acting as strong lenses to background sources (e.g. Bolton et al. 2006), and so mass census of the galaxy population using this technique is similarly limited.

Kinematics of the baryonic components can also provide robust estimates of the total enclosed mass of galaxies, since they directly trace the total gravitational potential (irrespective of the specific combination of baryons and DM). However, measuring kinematics requires spectroscopy with relatively high signal-to-noise ratio (S/N), which is considerably more expensive than photometry, especially at the redshift of typical strong-lens systems. This requirement tightens with increasing generality of the dynamical model employed.

Comparing the measurements of the projected enclosed mass for the same galaxy provides a critical test of these two techniques, and consequently whether previous works using either technique are directly comparable. Dynamical models have in fact been applied to a sample of lensed galaxies, finding that models with DM better match the lensing analyses compared to mass-follows-light models (Thomas et al. 2011). Using the lens sample from the Sloan Lens ACS Survey (SLACS; Bolton et al. 2006), two-integral dynamical

⋆ E-mail: adriano.poci@durham.ac.uk

Table 1. Physical properties of SNL-1 from the literature and this work.

Redshift	z	0.0312	Smith et al. (2015)
Einstein radius	θ_{Ein}	2.38 arcsec	Smith et al. (2015)
		1.48 kpc	
Total mass	$\log_{10}(M/\mathrm{M}_\odot)$	10.98	Collier et al. (2018)
Distance	D	132 Mpc	Co-moving
		128 Mpc	Angular diameter
Effective radius	R_{e}^{F814W}	3.49 arcsec	–
		2.15 kpc	

models were explored using spatially resolved stellar kinematics (Czoske et al. 2008; Barnabè et al. 2009, 2011). However, given the relatively large distances to the majority of strong lens galaxies (for instance, SLACS sample is at $0.08 < z < 0.35$, with the most massive around $z \sim 0.25$), the available data make detailed dynamical modelling challenging. These analyses (e.g. Treu & Koopmans 2004; Koopmans et al. 2009; Auger et al. 2010; Thomas et al. 2011) more often rely on mass estimators which require only a central velocity dispersion (such as in Cappellari et al. 2006; Wolf et al. 2010; Campbell et al. 2017, and their respective assumptions). The sample of lenses collected as part of the SINFONI Nearby Elliptical Lens Locator Survey (SNELLS; Smith, Lucey & Conroy 2015) is unique for the relatively small distances to the lens galaxies. Newman et al. (2017) have exploited their proximity to derive combined constraints from stellar-population and lensing analyses for a subset of the SNELLS galaxies in order to measure potential variations of the stellar initial mass function (IMF).

In this work, we also take advantage of the distances of the SNELLS galaxies to conduct a detailed dynamical analysis and comparison to constraints from lens modelling for SNL-1 (ESO286-G022). We compute triaxial three-integral orbit-based dynamical models of SNL-1 using the measured spatially resolved kinematic moments which do not require specific assumptions regarding the mass distribution or orbital anisotropy. For consistency with the lens modelling of Collier et al. (2018) – to which we directly compare the dynamical modelling results – we assume the cosmology of the *Wilkinson Microwave Anisotropy Probe* (*WMAP*) 7-yr experiment (Komatsu et al. 2011). Physical properties of SNL-1 are summarized in Table 1.

2 DATA AND TARGET

The dynamical model used in this work (Section 3) requires high-quality photometry and spectroscopy in order to be robustly constrained. We utilize *Hubble Space Telescope* (*HST*) Advanced Camera for Surveys (ACS) photometry in order to derive a model for the projected surface brightness of SNL-1, which is used as the tracer distribution for the dynamical model. Very Large Telescope (VLT) Multi-Unit Spectroscopic Explorer (MUSE) integral-field unit (IFU) spectroscopy is used to measure the stellar kinematics and star formation history. The stellar kinematics will constrain the dynamical model directly, while the stellar populations will be used to derive a stellar mass model from the surface brightness.

2.1 Photometry

Collier et al. (2018) presented observations of SNL-1 in the *F*336*W* and *F*814*W* bands of *HST*/ACS. From these data, we utilised the *F*814*W* band with an exposure time of 1050 s, as it is deeper than the
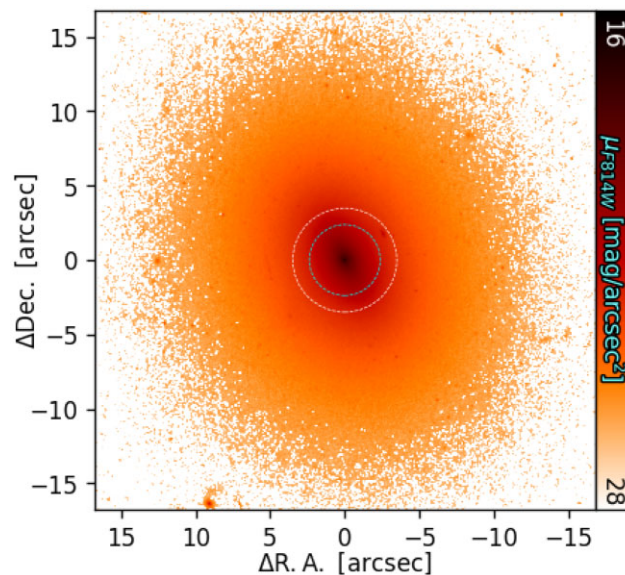

Figure 1. *F*814*W* image of SNL-1. Circular apertures with radii R_{e} and θ_{Ein} are shown in white and cyan, respectively.

*F*336*W* and consistent with the wavelength range of the spectroscopy. The *F*814*W* image is shown in Fig. 1. We also have *r*-band data from FORS2 which we utilize for auxiliary investigations below. However, given the lower spatial resolution and non-uniform sky background of this data, we opt for the *HST F*814*W* for the main modelling of this work.

2.2 Spectroscopy

The spectroscopy of SNL-1 was obtained using MUSE in the wide-field mode (WFM) configuration without adaptive optics, with program ID 0100.B-0769(A). These data have an exposure time of 1180 s. They were reduced via the standard ESO MUSE pipeline. At the derived distance to SNL-1, the 0.2 arcsec pixel^{-1} resolution of these data translate into a physical spatial resolution of 124 pc, but with an estimated point spread function (PSF) of ~ 1 arcsec (~ 621 pc) full width at half-maximum.

The MUSE data-cube was spatially binned to a target signal-to-noise ratio S/N = 50, using a PYTHON implementation[1] of the Voronoi binning algorithm (Cappellari & Copin 2003). This S/N was chosen as a compromise between being able to robustly extract higher-order information from the spectral fits, and maintaining sufficient spatial sampling across the FOV in order to preserve the

---

[1] Available at https://pypi.org/project/vorbin/.

kinematic structures. For all data products, we consider the rest-frame spectral range $\lambda \in [4700, 6700]$ Å, as red-ward of 6700 Å, the data are more noisy and contain sky emission lines. The binned data extend out to $r_{max} = 9.67$ arcsec (6.01 kpc) or $\sim 2.7\, R_e$. To measure the stellar population properties, the binned spectra were fit using the E-MILES[4] single stellar population (SSP) templates (Vazdekis et al. 2016) within PPXF[2] (Cappellari 2008, 2017). Specifically, we used the models computed using the 'BaSTI' isochrones (Pietrinferni et al. 2004), with 'base' (Solar neighbourhood) elemental abundances, and a fixed 'revised' Kroupa (2001) IMF over the safe ranges of age (t) and total metallicity ([Z/H]).[3] We included a multiplicative polynomial of order 12 to account for any mismatch between the absolute flux calibrations of the data and models, and any residual stellar continuum not accounted for by the models. A linear regularization term ($\Delta = 10$) was also included, which favours a smooth SSP weight distribution in the underlying $t - $ [Z/H] space given otherwise degenerate solutions.

We used the resulting distribution of age and metallicity in each spatial bin to compute the $F814W$-band stellar mass-to-light ratio ($M \star / L_{F814W}$). For the stellar mass, the E-MILES predictions including the mass in stars and stellar remnants was used. To compute the luminosity, we used the SSP model spectra directly. First, we took each SSP template which was assigned non-zero weight in the fit, and computed the absolute magnitude by applying the $F814W$ filter response curve redshifted to the distance of SNL-1. We then took the standard Solar spectrum of Colina, Bohlin & Castelli (1996) from the *HST* CALSPEC database (Bohlin, Gordon & Tremblay 2014; Bohlin, Hubeny & Rauch 2020) and computed its magnitude in the same way. In this way, we computed the total luminosity by weighting the individual SSP luminosities according to the weights of the spectral fit. The 2D map of $M \star / L_{F814W}$ is shown in the inset of Fig. 2.

Measurements of the stellar kinematics were also made from the same data, in this instance fitting the spectra again in PPXF using the MILES[4] empirical stellar library (Sánchez-Blázquez et al. 2006; Falcón-Barroso et al. 2011). We employ stellar spectra for this fit because they have higher intrinsic resolution compared to the SSP models, which improves the fit to complex absorption-line shapes. In this instance, an additive polynomial of order 12 was included to ensure that the shapes of the absorption features are accurately reproduced, and no regularization of the weights is imposed. In order to robustly constrain the dynamical model (Section 3), we measured the first four Gauss–Hermite moments of the line-of-sight velocity distribution (LOSVD), shown in the top row of Fig. 3.

During the fit to every spectrum, bad spectral pixels were iteratively clipped. This efficiently masks emission (which is not accounted for in the fitting), any sky lines, and other spurious artefacts in the spectrum. This scheme would also account for any emission from the source galaxy, as well as template mismatch during the fitting. Since the lensed images are undetected in continuum, no spatial masking is required.

3 DYNAMICAL MODEL

In this work, we aim to construct an accurate dynamical model in order to derive constraints that are in line with those produced from
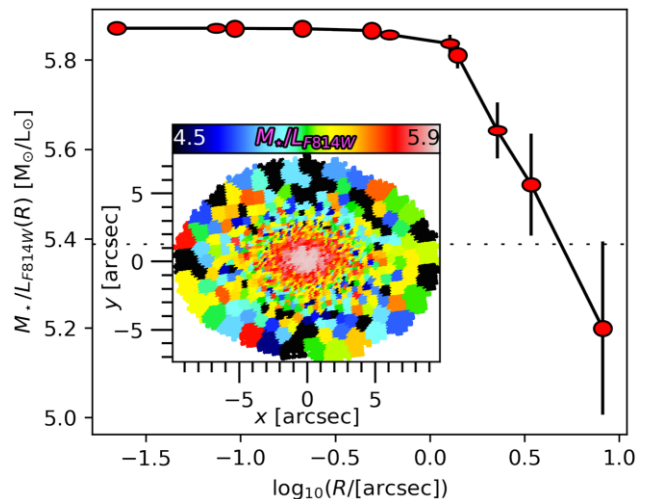

Figure 2. *Main:* Azimuthally sampled radial profile of the measured $M \star / L_{F814W}$ from the full spectral fitting in Section 2.2. The measurements are sampled in a thin annulus around the location (σ) of every Gaussian of MGE$_\mu$ (see the text). The data points depict the shape of the annulus taken for each Gaussian component, governed by its axial ratio. The vertical 'errorbars' illustrate the range of $M \star / L$ within each annulus. The black dashed line shows the average value of $M \star / L_{F814W}$ over the individual Voronoi bins. *Inset:* The spatially resolved map of $M \star / L_{F814W}$.

the lensing analysis. Since the latter is subject to few assumptions, we also wish to minimize those imposed on the dynamical model. We therefore apply a highly general orbit-superposition technique built on the original premise of Schwarzschild (1979). We utilize the triaxial three-integral implementation described in van den Bosch et al. (2008), van de Ven, De Zeeuw & Van Den Bosch (2008), Zhu et al. (2018a), and validated on mock data in Jin et al. (2019). This technique allows for freedom in the shape of the velocity ellipsoid and intrinsic mass distribution. Confronting this method with the result from lensing provides a critical test of the ingredients that are required to fit the observational data. We first briefly describe those ingredients here.

3.1 Projected mass model

Dynamical models require a description of the mass distribution in order to compute kinematic predictions, but this is not a direct observable. In practice, the mass distribution is derived from some projected constraints, then deprojected into an intrinsic distribution via specific assumptions about the shape of the galaxy. In this work, we computed a model of the projected surface brightness by fitting a multi-Gaussian Expansion (MGE; Monnet, Bacon & Emsellem 1992; Emsellem et al. 1994) to the $F814W$ photometry using a PYTHON implementation[5] (Cappellari 2002). To convert this fit into physical units, we took into account the surface-brightness dimming due to redshift, Galactic extinction according to Schlafly & Finkbeiner (2011), as well as a K-correction in the redshifted $F814W$ band. This model describes the projected distribution of the visible tracer of the underlying gravitational potential. Since it describes the surface brightness, we refer to it as MGE$_\mu$.

We still require, however, a description of the mass. To this end, we utilize the spectroscopic $M \star / L_{F814W}$ in order to convert the

[2]Available at https://pypi.org/project/ppxf/.

[3]as defined at http://research.iac.es/proyecto/miles/pages/ssp-models/safe-ranges.php.

[4]Available at http://research.iac.es/proyecto/miles/.
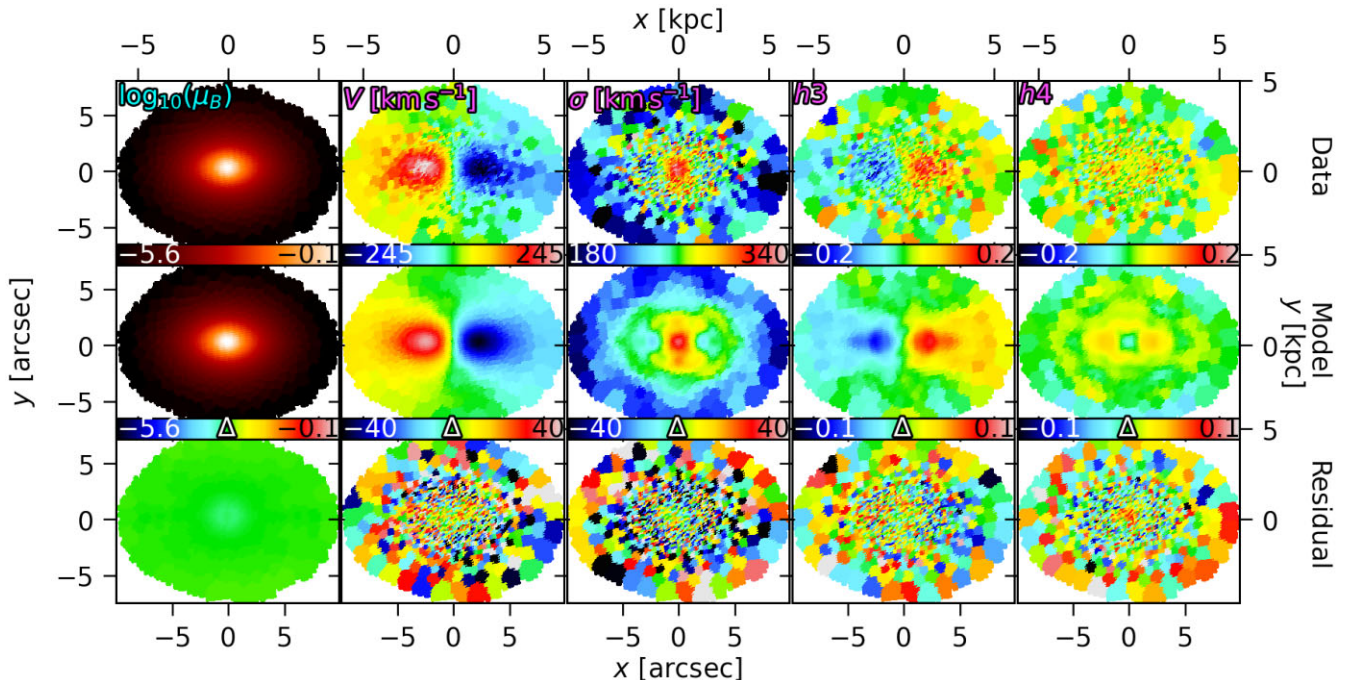
[5]Available at https://pypi.org/project/mgefit/.

Figure 3. Schwarzschild model fit to the measured kinematics of SNL-1. Data are shown in the top row and the model in the middle row. The residuals ($\Delta =$ data − model) are shown in the bottom row, with their corresponding colour bars. From left to right, the columns contain the projected surface brightness, mean velocity, velocity dispersion, $h3$, and $h4$.

stellar luminosity into mass. This is achieved following the approach of Poci, Cappellari & McDermid (2017), which we outline here (with similar approaches from Li et al. 2017; Mitzkus, Cappellari & Walcher 2017; Yang et al. 2020). Since MGE_μ is constructed from the co-addition of overlapping 2D Gaussians of different projected shapes, widths, and intensities, we derived the corresponding $M \star /L$ for each Gaussian individually. For each Gaussian, we took a thin projected annulus centred at its 'width' (radial extent) and with the same axial ratio, and calculated the mean $M \star /L$ from the PPXF stellar-population fit within that annulus. The mean value is then the factor that converts the luminosity of that Gaussian into mass. The final set of scaled Gaussians represents a projected mass model, which we denote MGE_Σ. In this implementation, the tailored azimuthal sampling naturally accounts for the interplay between the individual Gaussians and the changing shape of the light distribution with radius. This allows the dynamical model to account for the spatial variations of $M \star /L$ driven by age and metallicity variations, notwithstanding the evidence for internal IMF variations in massive ETGs similar to SNL-1 (e.g. van Dokkum et al. 2017; Vaughan et al. 2018; La Barbera et al. 2019). Given the spheroidal geometry of SNL-1, we expect radial profiles to capture these variations. The 2D map and resulting radial profile of the measured $M \star /L_{F814W}$ are shown in Fig. 2, and both MGE_μ and MGE_Σ are tabulated in Appendix A. With respect to the spatially averaged value denoted in Fig. 2, it can be seen that explicitly including the radial profile in our mass model accounts for the $\sim \pm 10$ per cent variations of $M \star /L_{F814W}$ caused by age and metallicity gradients.

3.2 Intrinsic parameter space exploration

The goal of the dynamical model is to find the best set of intrinsic (de-projected) properties that reproduce both the projected mass distribution and the observed (projected) stellar kinematics. The

specific implementation of the Schwarzschild method used here describes the intrinsic mass distribution with seven parameters:

(a) A parametrization of the intrinsic shape of the stellar component with three axis ratios $q = C/A$, $p = B/A$, and $u = A'/A$, where A, B, and C are the intrinsic major, intermediate, and minor axes, respectively, and A' is the projected major axis.

(b) The mass of the central SMBH, $M_\bullet$. This is implemented as a 'dark' mass following a Plummer density profile (Dejonghe 1987).

(c) Two parameters describing the DM halo, assumed to be a spherical Navarro–Frenk–White (NFW) model (Navarro, Frenk & White 1996). These are the concentration C_{DM} and dark mass fraction at r_{200}, f_{DM}.

(d) A global dynamical mass-to-light ratio. We denote this quantity Υ to distinguish from the spectroscopic $M \star /L$. Υ deepens or flattens the global gravitational potential, resulting in larger or smaller velocities, respectively, as needed to fit the kinematics. It can account for systematic effects caused by the absolute calibration of the SSP models, the particular choice of IMF, and/or the assumption of a spherical NFW DM halo.

For a single set of the above parameters, a large library of representative orbits are numerically integrated within the corresponding gravitational potential. The orbits conserve three integrals of motions: E, I_2, and I_3. Our models sample these integrals in 25 logarithmic steps for E, 18 linear steps for I_2, and 10 linear steps for I_3. To avoid discreteness (aliasing) in the models, each (E, I_2, I_3) location was 'dithered' (as in Cappellari et al. 2006) by a factor of 5. This creates a cloud of orbits with adjacent initial conditions for every integration, alleviating any possible discreteness in the model observables without having to integrate five times as many orbits.

The complete orbit library was fit to the measured kinematics via a non-negative least-squares (NNLS; Lawson & Hanson 1995) algorithm. As a boundary constraint, the orbits are also required to

Table 2. Free parameters of the Schwarzschild model, their best-fitting values, and the associated uncertainties which are derived as per Appendix B. Note that θ', ϕ', ψ' are derived from the best-fitting q, p, u.

Parameter	Description	Best	1σ
$\log_{10}(M_\bullet / \mathrm{M}_\odot)$	Black-hole mass	9.36	1.089
q	Intrinsic shape	0.4949	0.0090
p	Intrinsic shape	0.8390	0.0281
u	Intrinsic shape	0.9910	0.0026
θ'	Viewing angle	88.05°	
ϕ'	Viewing angle	75.76°	
ψ'	Viewing angle	75.76°	
C_{DM}	DM concentration	21.00	2.67
$\log_{10}[f_{\mathrm{DM}}(r_{200})]$	DM fraction at r_{200}	2.00	0.094
Υ [$\mathrm{M}_\odot/\mathrm{L}_\odot$]	Global M/L	0.66	0.042

reproduce the projected luminosity (MGE_μ). During this fit, a linear regularization in imposed – analogous to that used for spectral fitting – in this case favouring smooth distributions in the orbital phase space (E, I_2, I_3). The result of the NNLS fit is a set of (luminosity) weights for all of the integrated orbits, whose weighted combination reproduces all of the kinematic observables.

It is then necessary to explore many possible sets of parameters – different intrinsic gravitational potentials – at each stage finding the best subset of orbits via NNLS. Each model consists of 6 gravitational parameters: $M_\bullet$, q, p, u, C_{DM}, and f_{DM}, where each set is evaluated in NNLS over a range of Υ (since changing Υ does not require re-integration of the orbits). We note here, however, that using the measured velocity dispersion within the effective radius, σ_e, and the $M_\bullet$–σ_e relation of Kormendy & Ho (2013), we estimate the radius of the sphere-of-influence for the given $M_\bullet$ to be $r = 0.12$ arcsec – well below the MUSE PSF. Therefore, while we leave $M_\bullet$ as a free parameter for completeness, we expect the constraints on it to be weak given our current data. The exploration of the parameter space is described in Appendix B. Overall, 7233 unique models were evaluated, and the best fit is shown in Fig. 3.

4 RESULTS

The parameters of the best-fitting Schwarzschild model are given in Table 2. The Schwarzschild model provides a plethora of intrinsic properties, including the 3D shapes of the mass distribution (defined by the parameters in Table 2) and velocity ellipsoid (defined by the specific orbit superposition). One of the important quantities for the test sought here is the projected mass enclosed within a circular aperture of radius θ_{Ein}. We compute this in the following way. Each spatial aperture of the kinematic data has an associated luminosity weighting, which is the summation over the weights of all orbits which cross that aperture. We converted the luminosity weights into total mass weights by adding an MGE parametrization of the best-fitting NFW halo to MGE_Σ, then dividing by MGE_μ. This scale factor was evaluated at every aperture so that we could compute the fractional dynamical mass from the model. The projected fractional mass weight within θ_{Ein}, f_{Ein}, was then computed by simply summing all apertures with circular (projected) radius $r \leq \theta_{\mathrm{Ein}}$. Then the enclosed dynamical mass was computed by combining and integrating the enclosed mass profiles of the stars, DM, and SMBH. We integrated these profiles up to the maximum radial extent of the kinematic data, r_{max}, producing an enclosed dynamical mass within the FOV, M_{FOV}. Finally, the projected dynamical mass within θ_{Ein} is given straight-
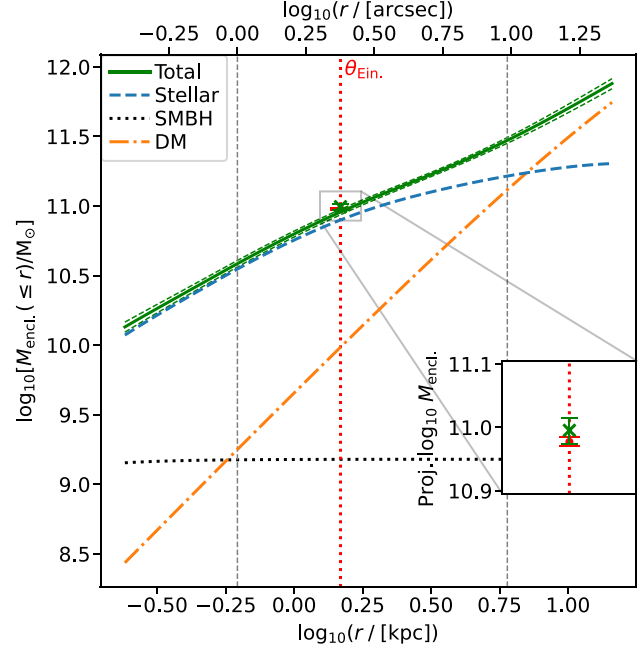

Figure 4. Enclosed mass of SNL-1. Intrinsic de-projected profiles of the enclosed stellar and dark mass are shown in dashed blue and dot–dashed orange, respectively. The total enclosed mass is shown as the green solid line [given by $M_\star(r) + M_{\mathrm{DM}}(r) + M_\bullet(r)$, although the SMBH is a point source over the radial range considered]. The black hole mass is shown in dotted grey for reference. The green cross and the red errorbar illustrate the projected constraints from the dynamical and lensing models, respectively. The PSF and largest radial extent of the MUSE data are demarcated by the inner and outer vertical dashed lines, respectively. θ_{Ein} is shown as the red dotted line. For the dynamical model, the errorbar on the cross and the dashed green lines illustrate the spread of all models within 1σ of the best-fitting solution. *Inset*: Zoom-in of the measurements of the projected Einstein mass from the lensing and dynamical models.

forwardly as $M_{\mathrm{Ein}} = f_{\mathrm{Ein}} M_{\mathrm{FOV}}$. The intrinsic enclosed mass profiles, along with the projected measurements from both the dynamical and lensing models, are presented in Fig. 4.

From the inset of Fig. 4, it is clear that the measurements of the projected Einstein mass from the lensing and dynamical models are in excellent agreement with one another, with $(9.49 \pm 0.15) \times 10^{10}\,\mathrm{M}_\odot$ and $(9.89 \pm 0.47) \times 10^{10}\,\mathrm{M}_\odot$, respectively. The uncertainty on the result from the dynamical model is computed by repeating the measurement for every model evaluation within 1σ of the best-fitting solution and finding the variance. While the dynamical mass is expected to be a robust quantity, this outcome is still reassuring in light of the generality and complexity of the Schwarzschild model, and given that the lensing and dynamical masses were completely independent of one another. By establishing that the Schwarzschild model is accurately anchored to the lensing result at θ_{Ein}, we can then confidently explore the other properties and spatial regions of the model in more detail. The intrinsic enclosed mass profiles shown in Fig. 4 illustrate that SNL-1 is completely baryon-dominated within θ_{Ein}. Enclosed within r_{max}, we measure a total stellar mass of $\log_{10}(M_{[\star]}/\mathrm{M}_\odot) = 11.23$, and a dynamical mass of $\log_{10}(M_{\mathrm{dyn}}/\mathrm{M}_\odot) = 11.41$. Enclosed within R_e, we measure $\log_{10}(M_{[\star]}/\mathrm{M}_\odot) = 11.01$ and $\log_{10}(M_{\mathrm{dyn}}/\mathrm{M}_\odot) = 11.07$, implying a DM fraction $f_{\mathrm{DM}}(r \leq R_e) = 10.67$ per cent. It is clear that SNL-1 is baryon-dominated within the spectroscopic FOV.
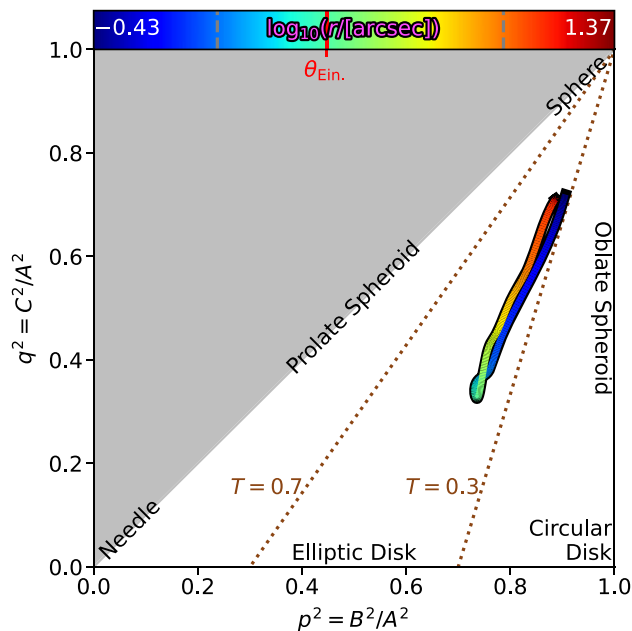
Figure 5. Correlations of the axis ratios of the intrinsic stellar mass distribution. The curve is coloured by radius. The PSF and largest radial extent of the MUSE data are demarcated on the colour bar by the dashed grey lines. θ_{Ein} is also marked on the colour bar. The dotted brown lines illustrate the boundaries between the classes of triaxiality in Jin et al. (2020). The various shape labels are borrowed from de Zeeuw & Schwarzschild (1989). The radial profile illustrates that SNL-1 tends towards a spherical mass distribution at both small and large radii, but exhibits the strongest departure at $\theta_{Ein.}$. Mild, approximately-constant triaxiality is present throughout the galaxy.

The intrinsic shape of SNL-1 is explored in Fig. 5 as a function of radius. This figure shows the radial dependence of the correlation between p^2 and q^2. In this way, the gradient of the curve is also approximately related to the triaxiality parameter (Franx, Illingworth & de Zeeuw 1991), $T \equiv (1 - p^2)/(1 - q^2)$. Strictly, our model of SNL-1 is triaxial at all radii. However $p = B/A \gtrsim 0.9$ for all radii implying only minor triaxiality. Jin et al. (2020) quantitatively categorises galaxies as oblate-triaxial, triaxial, and prolate-triaxial for $T < 0.3$, $0.3 < T < 0.7$, and $0.7 < T$, respectively. The mean triaxiality within the FOV for our model of SNL-1 is $\langle T \rangle = 0.39$, implying that is it oblate-triaxial. Interestingly, q is smallest around $\theta_{Ein.}$. This also happens to be the region in which the stellar rotation is high, and regularly-rotating galaxies are expected to be oblate (Weijmans et al. 2014), so the value of q is perhaps unsurprising. The outskirts become more spheroidal, coincident with where the rotation diminishes. This could be the result of isotropic minor accretion. Galaxies as massive as SNL-1 are expected to have accreted a large portion of their present-day mass (Oser et al. 2010; Khochfar et al. 2011; Lackner et al. 2012; Rodriguez-Gomez et al. 2016), which would preferentially settle in the outskirts (Karademir et al. 2019) and explain both the intrinsic shape and lack of rotation.

Of further interest is the shape of the intrinsic stellar velocity ellipsoid (SVE). This is particularly important because some dynamical mass estimators – which may also be used in joint lensing analyses – are valid only under the assumption of orbital isotropy. Orbital anisotropy has, however, been indirectly investigated in some lensing studies (e.g. Koopmans et al. 2009). To test this assumption, we investigate the radial variations of anisotropy for each pair of axes of a cylindrically aligned SVE. We explore the classic anisotropy
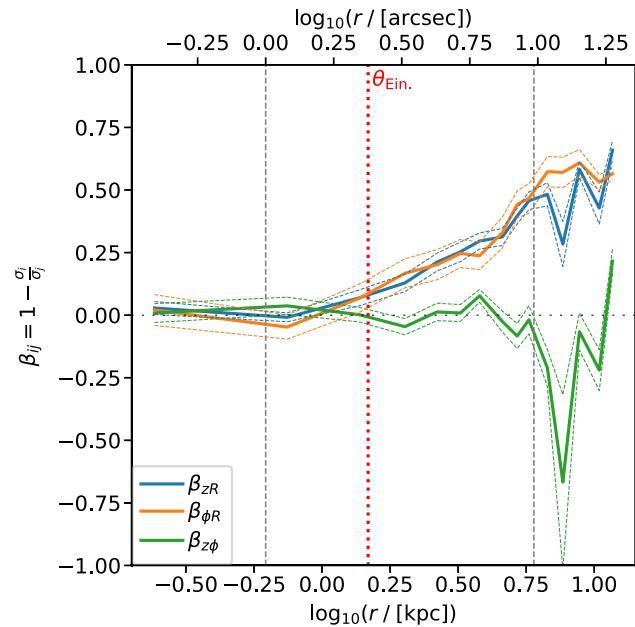

Figure 6. Radial profiles of the intrinsic axes of the stellar velocity ellipsoid. The β_{ij} quantities are defined in equation (1). The PSF and largest radial extent of the MUSE data are demarcated by the inner and outer vertical dashed lines, respectively. $\theta_{Ein.}$ is shown as the red dotted line. The coloured dashed lines illustrate the spread of all models within 1σ of the best-fitting solution. SNL-1 is approximately isotopic in the central regions ($r < \theta_{Ein}$), while the outskirts are characterized by an intrinsically oblate and anisotropic SVE.

parameter (Binney & Tremaine 1987)

$$\beta_{ij} = 1 - \frac{\sigma_i}{\sigma_j} \qquad (1)$$

for every $(i, j) \in [R, \phi, z]$. These results are shown in Fig. 6. Within $\theta_{Ein.}$, SNL-1 may be considered approximately isotropic; $\sigma_R \approx \sigma_\phi \approx \sigma_z$ for $r < \theta_{Ein.}$. At larger radii, SNL-1 becomes increasingly radially biased with increasing radius; $\sigma_z \approx \sigma_\phi < \sigma_R$ for $r > \theta_{Ein.}$. Such anisotropy provides additional evidence of a rich accretion history over which many systems contributed to the build-up of the outer spheroid (e.g. Naab, Khochfar & Burkert 2006), as has also been found in the Milky-Way (e.g. Helmi et al. 2018). It also indicates that within θ_{Ein}, the assumption of orbital isotropy – at least for SNL-1 – would be reasonable.

5 DISCUSSION

The dynamical model has afforded us a detailed look at the resolved internal kinematic properties of SNL-1. We see that the central regions exhibit high rotation, an oblate mass distribution, and approximately isotropic orbits. The outskirts exhibit little-to-no rotation, a spheroidal mass distribution, and are accompanied by an increase in radially biased orbits. Intermediate triaxiality persists throughout the galaxy.

5.1 SNL-1 in context

Apart from being a strong lens, SNL-1 exists within the population of massive elliptical galaxies. It is, however, highly compact for its mass (Campbell et al. 2014; Smith et al. 2015; Spiniello et al. 2015), and therefore may not be representative of the ETG population as
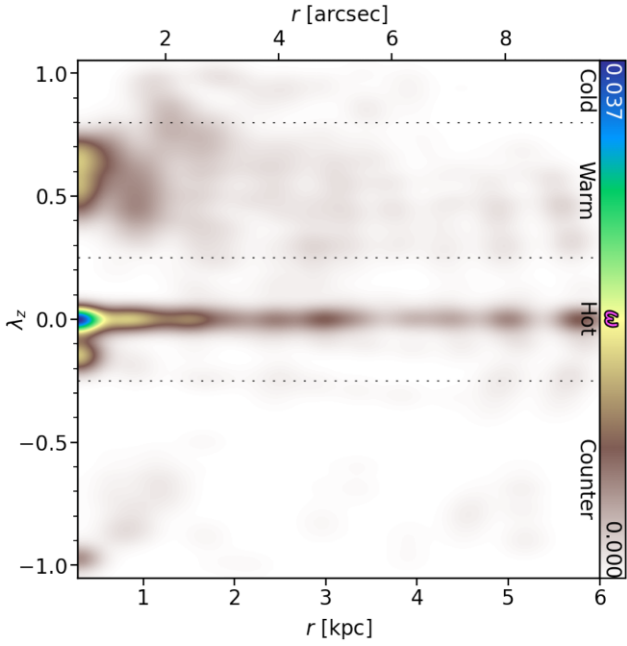
Figure 7. Circularity distribution of the best-fitting Schwarzschild model within the spectroscopic FOV. The colour shows the orbital weight as a function of circularity and radius. The black dashes lines show the separation into four broad dynamical components (see the text). SNL-1 contains predominantly dynamically hot orbits at all radii. The inner rotating 'disc' is visible for $r \lesssim 2$ kpc and $\lambda_z \sim 0.6$. There is also the suggestion of counter-rotating orbits, though these contribute little mass.

a whole. We thus seek to compare it to similar galaxies in order to discern any differences between them. Exploiting the generality of the Schwarzschild model, we can make this comparison for a number of key intrinsic properties.

In Fig. 7, the orbital circularity distribution is shown. The orbital circularity λ_z is a measure of the intrinsic angular momentum around the short axis of the mass distribution (Zhu et al. 2018a). It is normalized by the angular momentum of a circular orbit with equivalent energy, such that $\lambda_z \in [-1, 1]$, representing counter- and co-rotating circular orbits, respectively. Box and/or radial orbits will exhibit $\lambda_z \sim 0$. Fig. 7 shows that SNL-1 is composed of dynamically-hot and -warm orbits with $\lambda_z \lesssim 0.7$. We use this distribution to compare to the analysis conducted on the representative sample of nearby galaxies from the CALIFA survey (Sánchez et al. 2012), which contains a small number of galaxies of similar mass to SNL-1. Zhu et al. (2018b) applied triaxial Schwarzschild models to that sample and analysed the distribution of orbits as a function of stellar mass by dividing the circularity into broad bins of 'cold' ($\lambda_z \geq 0.8$), 'warm' ($0.25 < \lambda_z < 0.8$), 'hot' ($|\lambda_z| \leq 0.25$), and counter-rotating ($\lambda_z < -0.25$) orbits. They specifically considered the fractions of each orbit type within R_e. Applying these same criteria, we compare orbits fractions to the CALIFA galaxy sample in Fig. 8. The model of SNL-1 reveals cold, warm, hot, and counter-rotating fractions within R_e of 0.07, 0.47, 0.39, and 0.07, respectively. SNL-1 is consistent with the $\log_{10}(M_{[\star]}/M_\odot) \sim 11$ population of galaxies from CALIFA, in terms of the orbit distributions. Given its mass, SNL-1 is expected to be supported predominantly by random motions (for instance, see Cappellari et al. 2013a), and we see this borne out of our model as a significant fraction of hot orbits at all radii. Simultaneously, SNL-1 exhibits relatively high peak rotation velocity. It can be seen from Fig. 7 that this rotation is produced predominantly by the cloud of
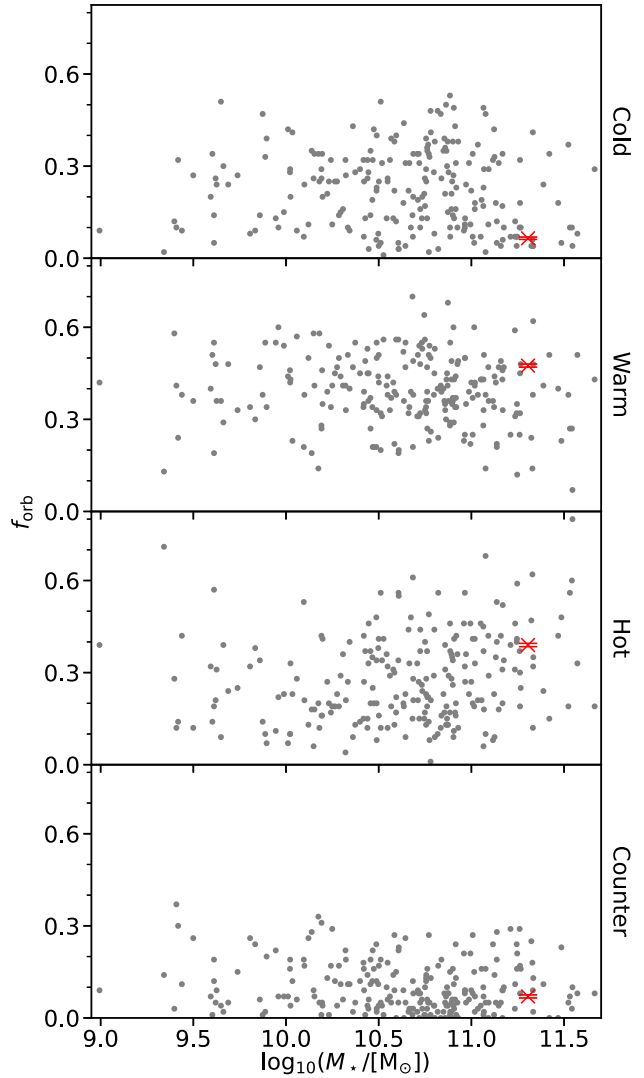

Figure 8. Orbit fractions as a function of stellar mass. The grey dots show the fractions of cold, warm, hot, and counter-rotating orbits (top to bottom) from Zhu et al. (2018b) for the CALIFA sample. The corresponding values from the dynamical model of SNL-1 are marked by the red crosses. The illustrated uncertainty is the spread of all models within 1σ of the best-fit.

dynamically warm orbits extending from the centre to $\sim$2kpc (since there is negligible contributions from cold orbits), thereby explaining the relatively high warm-orbit fraction within R_e. These orbits would constitute a 'thick-disc'-like component, embedded in the otherwise spheroidal galaxy.

In contrast to its rather typical dynamical properties, SNL-1 appears to be somewhat unusual structurally, being highly compact for its mass. We therefore investigate its position on the mass–size plane, an empirical correlation believed to capture the various evolutionary stages of a population of galaxies (e.g. Newton et al. 2011; Cappellari et al. 2013a; Cappellari 2013; Scott et al. 2017; Krajnović et al. 2018; Li et al. 2018). In Fig. 9, we place SNL-1 on both the dynamical-mass–size plane measured in Li et al. (2018) using the MaNGA survey (Bundy et al. 2015), and the stellar-mass–size plane using DR3 (Croom et al. 2021) of the SAMI survey (Croom et al. 2012), comparing also to a sample of 'relic' galaxies from the INSPIRE survey (Spiniello et al. 2021). SNL-1 occupies the boundary at the compact, high-mass edge of the 'normal' galaxy
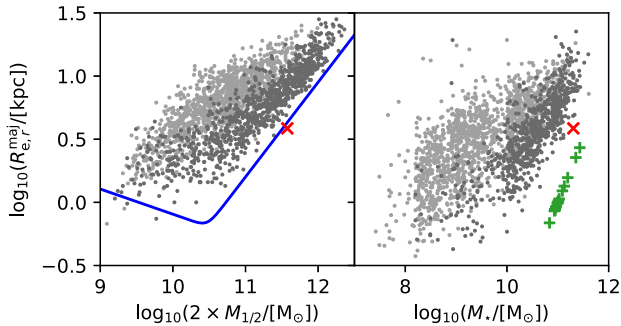
Figure 9. Mass–size plane projections for two different literature samples. *Left:* The dynamical mass and the effective radius along the major axis R_{e}^{maj} for the MaNGA sample (Li et al. 2018). $M_{1/2}$ is the dynamical mass enclosed within the 3D spherical half-light radius $R_{1/2}$. The blue line shows the 'zone of exclusion' of Cappellari et al. (2013b). *Right:* The total stellar mass and the effective radius along the major axis R_{e}^{maj} for the GAMA subset (non-cluster galaxies) of the SAMI sample (Croom et al. 2021). The green plus symbols show the sample of 'relic' galaxies from the INSPIRE survey (Spiniello et al. 2021). In both panels, the samples are coloured by morphological type; late-type galaxies are light grey ('S' from MaNGA and `VisualMorphol-ogyDR3.TYPE` ≥ 2.0 for SAMI), and earlier morphological types are dark grey. In both panels, the corresponding measurement from the dynamical model of SNL-1 is marked by the red cross. The sizes from both surveys are *r*-band measurements. We compute an *r*-band effective radius for SNL-1 from FORS2 photometry of $R_{e,r}^{maj} = 5.98''$ (3.83 kpc). In both panels, SNL-1 lies at the compact, high-mass edge of the general galaxy populations.

populations. It resides in the 'zone of exclusion', which was derived dynamically for the ATLAS³ᴰ sample of galaxies in the Virgo cluster (Cappellari 2013, but proposed originally by Bender, Burstein & Faber 1992; Burstein et al. 1997). This may be the result of the fact that more compact galaxies are preferentially easier to detect as being strong lenses, as already hinted to in the results of Newton et al. (2011). Moreover, SNL-1 appears to bridge the gap between the relic and non-relic populations, the former being defined specifically by their compactness. This further reinforces the atypical compactness of SNL-1 with respect to the broader galaxy population.

Overall, this section has shown that SNL-1 is dynamically typical but structurally atypical compared to galaxies of similar mass. Of particular interest for lensing models which utilize the central velocity dispersions as dynamical tracers, at its Einstein radius SNL-1 exhibits the greatest departure from a spherical mass distribution, but no significant departure from orbital isotropy. These results suggest that orientation/configuration biases are likely already manifest in existing lensing samples, while our methodology – specifically the sophisticated orbit-based dynamical models – provides a way to quantify and account for such biases in future samples. In this case, the properties derived from lensing analyses, even if large samples are collected, may not be representative of the broader galaxy population.

5.2 Dynamical analyses of lensing systems

The lensing selection function is of considerable importance, and depends on the projected mass of the lens along the LOS (for which the stellar velocity dispersion is a common proxy; Treu et al. 2010). However, there are other physical properties of the lensing galaxies that would be especially conducive to producing detectable strong-lens signals. For instance, Schaller et al. (2015) studied a sample of galaxy clusters in cosmological hydrodynamical simulations and find that, of their six clusters, four brightest cluster galaxies are

prolate, and two are oblate. They argue that if such galaxies were intrinsically prolate, but were selected for observation in such a way which favours end-on orientations, then the measured central velocity dispersion would be biased to higher values compared to a sample with a uniform distribution of orientations. A similar argument could apply in galaxy-scale lens systems, where internal structures such as bars could also play a role. Therefore, using the central velocity dispersion measurements as part of lens models would propagate this systematic bias and render the lensing sample non-representative. It is thus important to determine whether the selection function for lensing does indeed favour certain geometric configurations, and whether these configurations can be accurately reproduced in lens models.

It is to this end that dynamical models, such as those presented in this work, can provide insight. For example, the *u* parameter in this implementation of the Schwarzschild model describes the projection of a triaxial system. If strong lens galaxies have a tendency to be end-on triaxial systems, the distribution of *u* for a sample of lens galaxies will have a lower mean with respect to a mass-matched sample of non-lensed galaxies. Schwarzschild implementations that include treatment of figure rotation such as FORSTAND (Vasiliev & Valluri 2020) could simultaneously constrain the orientation of time-variable triaxial structures such as bars. However, as prefaced in Section 1, the sample of strong lens galaxies with spatially resolved stellar kinematics of sufficient quality is currently too small for a statistical analysis. Exploiting the adaptive-optics capabilities of upcoming facilities such as MAVIS (McDermid et al. 2020) and HARMONI (Thatte et al. 2016) will bring more distant strong lens galaxies into the regime amenable to this analysis.

Although a direct statistical test is not yet available, the existing mass models used by lensing analyses appear to agree with independent techniques. For instance, results from lensing show that the total-mass distributions of the lensing population exhibit a surprisingly strong tendency towards isothermal radial profiles – having $\gamma \sim -2.1$ for $\rho_{tot}(r) \propto r^{\gamma}$ (e.g. Treu & Koopmans 2004; Koopmans et al. 2009; Auger et al. 2010; Barnabè et al. 2011; Bolton et al. 2012; Sonnenfeld et al. 2013; Shajib et al. 2021), with an intrinsic scatter of order $0.1-0.2$ between them. This is in good agreement with direct modelling of the total mass distribution using Jeans models of the stellar kinematics (Tortora et al. 2014; Cappellari et al. 2015; Poci et al. 2017; Bellstedt et al. 2018; Li et al. 2019; Derkenne et al. 2021, despite different internal assumptions between them), cosmological simulations (Remus et al. 2013; Wang et al. 2019), and gas dynamical models (Serra et al. 2016), at least for $z \lesssim 0.5$ (Derkenne et al. 2021). Since these studies are on physically similar but non-lensed galaxies, this could imply at face value that there is no additional lensing selection bias beyond the velocity dispersion. However, by construction, assuming a single spherical power law for the total mass of galaxies (or even an oblate total-mass distribution; Poci et al. 2017) cannot account for triaxiality (or bars), and so this comparison cannot exclude the existence of such a bias.

We can calculate the total-mass profile slope from the dynamical model in this work by simply combining the best-fitting stellar and DM contributions. This is given in Fig. 10, presented on the same scheme as Fig. 4. Given the flexibility of the models used in this work, there is no guarantee that the resulting total-mass density should be accurately described by a single power law in radius. We therefore measure the mean logarithmic density slope within R_e given as

$$\gamma' = \frac{\log_{10}[\rho_{tot}(R_e)/\rho_{tot}(R_{in})]}{\log_{10}(R_e/R_{in})}, \qquad (2)$$
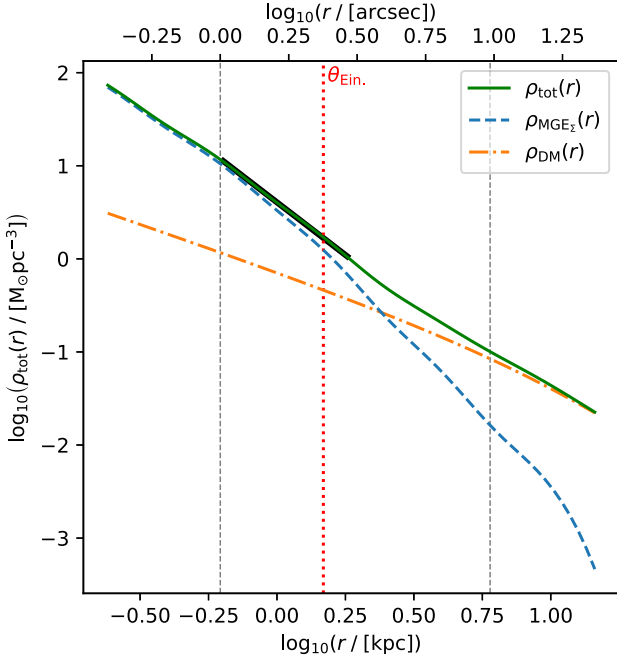
Figure 10. Density profiles for SNL-1 from the best-fitting Schwarzschild model. The total enclosed mass is shown in green [given by $M_\star(r) + M_{\mathrm{DM}}(r)$], the stellar mass is dashed blue, and the DM is dot–dashed orange. Underplotted in the thick black line is the single power-law $\rho_{\mathrm{tot}}(r) \propto r^{\gamma'}$ with the value of γ' measured from equation (2). SNL-1 does indeed have a mean logarithmic density slope which is close to isothermal over the fitted radial range. In addition, the black line illustrates that a power law is a good representation of the total-mass density for SNL-1 over the region it is measured.

where we set $R_{\mathrm{in}} = 1$ arcsec, the FWHM of the kinematic data. We measure a mean logarithmic slope of the total-mass density profile to be $\gamma' = 2.262 \pm 0.006$ (1σ uncertainty), which is within the distributions found in the aforementioned works from lensing, stellar and gas kinematics, and cosmological simulations. While in this work we do not constrain the total-mass directly like previous studies, Poci et al. (2017) showed that modelling the total-mass directly or considering stellar + DM contributions produce consistent results, while Barnabè et al. (2011) showed that the slopes of the total-mass profiles between Jeans models and (two-integral) Schwarzschild models agree.

Finally more broadly, we have derived a measurement of M_{Ein} from the Schwarzschild model which is in excellent agreement with that from the independent lensing constraints. This result justifies being able to leverage lensing constraints directly within dynamical models. Doing so would be especially useful when constraints from the stellar kinematics alone are limited – for instance, at higher redshift. Requiring any model to respect both the enclosed lensing mass and the kinematic constraints simultaneously would also allow degeneracies to be mitigated concerning implied gradients in M/L, among others.

5.3 Exploring different orientations

The Schwarzschild model is fully defined in 3D space, and is projected through the LOS only to compare to observations. We are therefore able to 'observe' this model at arbitrary orientations. In this section, we explore particular re-projections of the best-
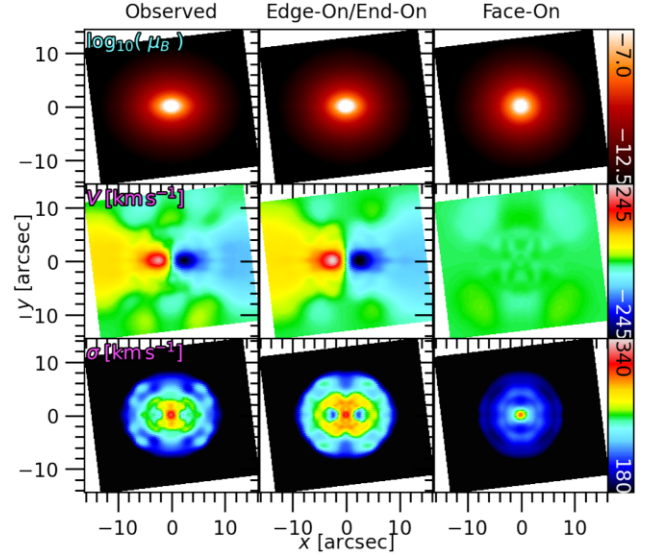

Figure 11. Re-projected Schwarzschild models of SNL-1. From top to bottom are the projected surface brightness, mean velocity, and velocity dispersion. From left to right, the viewing angles are: observed $(\theta, \phi, \psi) = (\theta', \phi', \psi')$; edge-on and end-on $(\theta, \phi, \psi) = (90°, 0°, \psi')$; face-on $(\theta, \phi, \psi) = (0°, 90°, \psi')$. The kinematics are shown simply for illustration, and align with the expectation for these viewing directions. The changes to the surface brightness (and correspondingly the mass density) allow us to probe the impact of particular viewing directions on the strength of the lensing signal.

fitting dynamical model, and their impact on the lensing properties. We show examples in Fig. 11. These figures are constructed by taking the distribution of orbits and their relative weights from the original Schwarzschild model, then 'observing' the model from the specified viewing direction. New LOSVD are computed from this viewing direction. The surface brightness and kinematics are then measured by integrating, and fitting a Gauss–Hermite function to, these LOSVD, respectively. Since the models are spatially binned for the sole purpose of comparing to observations, we explore these re-projections on a non-binned pixel grid, but maintaining the MUSE pixel scale of 0.2 arcsec pixel^{-1}.

We explore two projections in addition to the observed direction in Fig. 11, defined by their viewing angles: from left to right, $(\theta, \phi, \psi) = (\theta', \phi', \psi'); (\theta, \phi, \psi) = (90°, 0°, \psi'); (\theta, \phi, \psi) = (0°, 90, \psi')$. Primed angles refer to their observed values; that is, those derived from the best-fitting Schwarzschild model and given in Table 2. The additional projections correspond to what are expected to be the most and least dense along the LOS, and should therefore have the largest impact on the lensing cross-section. The kinematics exhibit changes which are expected for the different orientations; the edge-on projection shows the highest amplitude of rotation, which effectively vanishes in the face-on projection. The velocity dispersion also contains the signature of high rotation in the edge-on projection, with a depression along the mid-plane.

From the surface brightness of each projection, we compute the lensing cross-section by assuming a spatially constant $M\star/L$, and neglecting the small DM contribution within θ_{Ein} (discussed below). These are shown in Fig. 12. The face-on and edge-on/end-on projections exhibit a cross-section area which is $0.671\times$ and $1.165\times$ that of the observed projection. Conversely, we see only a ~ 10 per cent change in θ_{Ein} between the extrema. The edge-
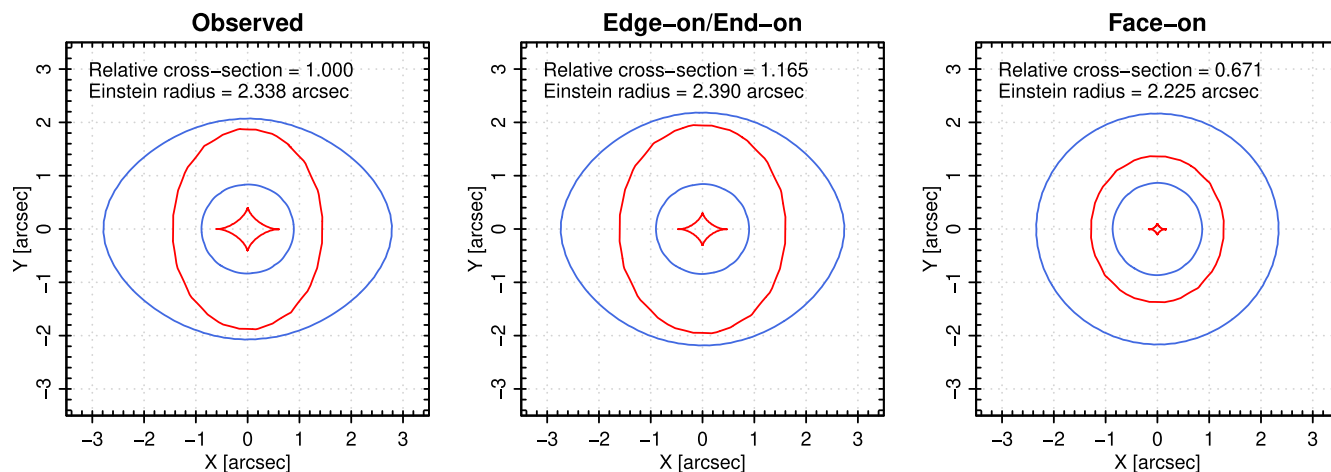
Figure 12. Lensing properties of SNL-1 for three different orientations, as computed from the re-projected dynamical models. From left to right is the observed, edge-on/end-on, and face-on projections. The surface densities have been rescaled to lensing convergence by a single constant factor which reproduces the observed Einstein radius in the observed orientation. The blue and red lines show the image-plane critical curves and source-plane caustics, respectively. The cross-section for lensing is given by the area inside the outer caustic: the cross-section in the observed orientation is close to that of the 'maximal-lensing' edge-on/end-on orientation, and substantially larger than the 'minimal-lensing' face-on case.

on/end-on relative cross-section is perhaps unsurprising, since the best-fit dynamical model has a corresponding inclination of $\sim 88°$. This implies that SNL-1 is already in a configuration which is close to its 'maximum' projection, and suggests that it was detected as a lens in SNELLS at least partially due to its favourable orientation. Moreover, the substantial change in lensing cross-section and central velocity dispersion for the different projections, with little change to θ_{Ein}, might also produce different inferred mass profiles from lensing techniques which utilize the central kinematics (e.g. Treu et al. 2010).

Applying a spatially-constant $M\star/L$ may impact the projected mass measurements for each orientation. We of course do not have access to the $M\star/L$ integrated along lines of sight other than the observed orientation. However, the radial geometry of the observed $M\star/L$ map (Fig. 2, inset) indicates that this geometry may hold for all projections. In that case, and since we are measuring the cross-sections relative to the observed orientation, applying the same $M\star/L(R)$ profile (such as the one measured in Fig. 2) to each projection will produce the same relative differences as a simple spatially constant $M\star/L$. Similarly, given the spherical NFW employed in the dynamical model, the DM also does not have an impact on the relative measurements for the re-projections.

6 CONCLUSION

We have explored general orbit-based dynamical models of the relatively-nearby strong-lens system SNL-1. We have compared our results directly to the measurements from lensing models, and investigated a host intrinsic properties. Our findings are summarized here:

(i) The enclosed mass measurements between the dynamical and lensing models agree well within their respective uncertainties, with $M_{\mathrm{Ein.}}^{\mathrm{lens}}/M_{\mathrm{Ein.}}^{\mathrm{Schw.}} = 0.96$. This result supports the conclusion from the lensing model that favoured a relatively dwarf-poor IMF such as Kroupa (2001) for the centre of SNL-1 (Smith et al. 2015). We

found that SNL-1 is baryon-dominated within the spectroscopic FOV, which encompasses both θ_{Ein} and R_e (Fig. 4).

(ii) SNL-1 appears to be oblate-triaxial and radially anisotropic in its outer regions (Figs 5 and 6). In general, models (lensing or otherwise) which attempt to separate the baryonic and DM contributions to the total mass need to be able to account for these physical properties.

(iii) Dynamically, SNL-1 is consistent with the broader galaxy population at fixed mass as traced by the CALIFA survey. Despite appearing to be a typical old, massive, red ETG, SNL-1 still exhibits relatively high rotation velocities in a central thick disc-like configuration. This is evidenced by the somewhat high proportion of kinematically warm orbits within R_e (Fig. 8).

(iv) In contrast, SNL-1 is markedly more compact at fixed mass compared to the MaNGA and (field) SAMI samples (Fig. 9). This compactness likely enhances the lensing signal compared to that of lower density galaxies even at fixed mass. Nevertheless, the shape of the mass density profile of SNL-1 is in good agreement with a wide range of galaxy samples (Fig. 10).

(v) Finally, we explored the impact of changing the observed orientation of a galaxy which is already known to be a lens. We find a substantial impact on the lensing cross-section of a factor of ~ 2 between the projected extrema. We find only a minor difference between the observed and maximal orientations, implying that the selection of SNL-1 as a lens may have been impacted by its observed orientation (Fig. 12).

We conclude that combing lensing and sophisticated orbit-based dynamical models will provide access to the intrinsic physical properties of galaxies in a robust manner. In anticipation of the increase in the number of suitable galaxies expected with upcoming facilities, we continue to investigate the ways in which lensing and dynamical analyses can complement one another.

DATA AVAILABILITY

The observational data used in this work are publicly available in the ESO archive (archive.eso.org). Other products can be provided upon reasonable request to the author.

REFERENCES

Astropy Collaboration et al., 2013, A&A, 558, A33
Auger M. W., Treu T., Bolton A. S., Gavazzi R., Koopmans L. V. E., Marshall P. J., Moustakas L. A., Burles S., 2010, ApJ, 724, 511
Barnabè M., Czoske O., Koopmans L. V. E., Treu T., Bolton A. S., 2011, MNRAS, 415, 2215
Barnabè M., Czoske O., Koopmans L. V. E., Treu T., Bolton A. S., Gavazzi R., 2009, MNRAS, 399, 21
Barone T. M. et al., 2022, MNRAS, 512, 3828
Behnel S., Bradshaw R., Citro C., Dalcin L., Seljebotn D. S., Smith K., 2011, Comput. Sci. Eng., 13, 31
Bellstedt S. et al., 2018, MNRAS, 476, 4543
Bender R., Burstein D., Faber S. M., 1992, ApJ, 399, 462
Binney J., Tremaine S., 1987, Galactic Dynamics. Princeton Univ. Press, Princeton, NJ
Bohlin R. C., Gordon K. D., Tremblay P.-E., 2014, PASP, 126, 711
Bohlin R. C., Hubeny I., Rauch T., 2020, AJ, 160, 21
Bolton A. S. et al., 2012, ApJ, 757, 82
Bolton A. S., Burles S., Koopmans L. V. E., Treu T., Moustakas L. A., 2006, ApJ, 638, 703
Bundy K. et al., 2015, ApJ, 798, 7
Burstein D., Bender R., Faber S., Nolthenius R., 1997, AJ, 114, 1365
Campbell D. J. R. et al., 2017, MNRAS, 469, 2335
Campbell L. A. et al., 2014, MNRAS, 443, 1231
Cappellari M. et al., 2006, MNRAS, 366, 1126
Cappellari M. et al., 2013a, MNRAS, 432, 1709
Cappellari M. et al., 2013b, MNRAS, 432, 1862
Cappellari M. et al., 2015, ApJ, 804, L21
Cappellari M., 2002, MNRAS, 333, 400
Cappellari M., 2008, MNRAS, 390, 71
Cappellari M., 2013, ApJ, 778, L2
Cappellari M., 2017, MNRAS, 466, 798
Cappellari M., Copin Y., 2003, MNRAS, 342, 345
Chae K.-H., 2003, MNRAS, 346, 746
Colina L., Bohlin R. C., Castelli F., 1996, AJ, 112, 307
Collier W. P., Smith R. J., Lucey J. R., 2018, MNRAS, 473, 1103
Cortese L. et al., 2014, ApJ, 795, L37
Croom S. M. et al., 2012, MNRAS, 421, 872
Croom S. M. et al., 2021, MNRAS, 505, 991
Czoske O., Barnabè M., Koopmans L. V. E., Treu T., Bolton A. S., 2008, MNRAS, 384, 987
de Zeeuw T., Schwarzschild M., 1989, ApJ, 345, 84
Dejonghe H., 1987, MNRAS, 224, 13
Derkenne C., McDermid R. M., Poci A., Remus R.-S., Jørgensen I., Emsellem E., 2021, MNRAS, 506, 3691
Emsellem E., Monnet G., Bacon R., Nieto J.-L., 1994, A&A, 285, 739
Falcón-Barroso J., Sánchez-Blázquez P., Vazdekis A., Ricciardelli E., Cardiel N., Cenarro A. J., Gorgas J., Peletier R. F., 2011, A&A, 532, A95
Franx M., Illingworth G., de Zeeuw T., 1991, ApJ, 383, 112
Gallazzi A., Charlot S., Brinchmann J., White S. D. M., Tremonti C. A., 2005, MNRAS, 362, 41
Harris C. R. et al., 2020, Nature, 585, 357
Helmi A., Babusiaux C., Koppelman H. H., Massari D., Veljanoski J., Brown A. G. A., 2018, Nature, 563, 85
Hunter J. D., 2007, Comput. Sci. Eng., 9, 90
Jin Y., Zhu L., Long R. J., Mao S., Wang L., van de Ven G., 2020, MNRAS, 491, 1690
Jin Y., Zhu L., Long R. J., Mao S., Xu D., Li H., van de Ven G., 2019, MNRAS, 486, 4753
Karademir G. S., Remus R.-S., Burkert A., Dolag K., Hoffmann T. L., Moster B. P., Steinwandel U. P., Zhang J., 2019, MNRAS, 487, 318
Khochfar S. et al., 2011, MNRAS, 417, 845
Komatsu E. et al., 2011, ApJS, 192, 18
Koopmans L. V. E. et al., 2009, ApJ, 703, L51
Kormendy J., Ho L. C., 2013, ARA&A, 51, 511
Krajnović D., Emsellem E., den Brok M., Marino R. A., Schmidt K. B., Steinmetz M., Weilbacher P. M., 2018, MNRAS, 477, 5327
Kroupa P., 2001, MNRAS, 322, 231
La Barbera F. et al., 2019, MNRAS, 489, 4090
Lackner C. N., Cen R., Ostriker J. P., Joung M. R., 2012, MNRAS, 425, 641
Lawson C. L., Hanson R. J., 1995, Solving Least Squares Problems: Classics in Applied Mathematics. Society for Industrial and Applied Mathematics
Li H. et al., 2017, ApJ, 838, 77
Li H. et al., 2018, MNRAS, 476, 1765
Li R. et al., 2019, MNRAS, 490, 2124
McDermid R. M. et al., 2020, preprint (arXiv:2009.09242)
Mitzkus M., Cappellari M., Walcher C. J., 2017, MNRAS, 464, 4789
Monnet G., Bacon R., Emsellem E., 1992, A&A, 253, 366
Naab T., Khochfar S., Burkert A., 2006, ApJ, 636, L81
Navarro J. F., Frenk C. S., White S. D. M., 1996, ApJ, 462, 563
Newman A. B., Smith R. J., Conroy C., Villaume A., van Dokkum P., 2017, ApJ, 845, 157
Newton E. R., Marshall P. J., Treu T., Auger M. W., Gavazzi R., Bolton A. S., Koopmans L. V. E., Moustakas L. A., 2011, ApJ, 734, 104
Oser L., Ostriker J. P., Naab T., Johansson P. H., Burkert A., 2010, ApJ, 725, 2312
Perez F., Granger B. E., 2007, Comput. Sci. Eng., 9, 21
Pietrinferni A., Cassisi S., Salaris M., Castelli F., 2004, ApJ, 612, 168
Poci A., Cappellari M., McDermid R. M., 2017, MNRAS, 467, 1397
Remus R.-S., Burkert A., Dolag K., Johansson P. H., Naab T., Oser L., Thomas J., 2013, ApJ, 766, 71
Rodriguez-Gomez V. et al., 2016, MNRAS, 458, 2371
Sánchez S. F. et al., 2012, A&A, 538, A8
Sánchez-Blázquez P. et al., 2006, MNRAS, 371, 703
Schaller M. et al., 2015, MNRAS, 452, 343
Schlafly E. F., Finkbeiner D. P., 2011, ApJ, 737, 103
Schwarzschild M., 1979, ApJ, 232, 236
Scott N. et al., 2017, MNRAS, 472, 2833
Seabold S., Perktold J., 2010, Python in Science Conference. Austin, TX, p. 92
Serra P., Oosterloo T., Cappellari M., den Heijer M., Józsa G. I. G., 2016, MNRAS, 460, 1382
Shajib A. J., Treu T., Birrer S., Sonnenfeld A., 2021, MNRAS, 503, 2380
Shu Y. et al., 2015, ApJ, 803, 71
Smith R. J., Lucey J. R., Collier W. P., 2018, MNRAS, 481, 2115
Smith R. J., Lucey J. R., Conroy C., 2015, MNRAS, 449, 3441

Sonnenfeld A., Treu T., Gavazzi R., Suyu S. H., Marshall P. J., Auger M. W., Nipoti C., 2013, ApJ, 777, 98

Spiniello C. et al., 2021, A&A, 646, A28

Spiniello C., Barnabè M., Koopmans L. V. E., Trager S. C., 2015, MNRAS, 452, L21

Thatte N. A. et al., 2016, Ground-Based and Airborne Instrumentation for Astronomy VI, Vol. 9908. International Society for Optics and Photonics, p. 99081X

Thomas J. et al., 2011, MNRAS, 415, 545

Tian Y., Cheng H., McGaugh S. S., Ko C.-M., Hsu Y.-H., 2021, ApJ, 917, L24

Tortora C., La Barbera F., Napolitano N. R., Romanowsky A. J., Ferreras I., de Carvalho R. R., 2014, MNRAS, 445, 115

Treu T., 2010, ARA&A, 48, 87

Treu T., Auger M. W., Koopmans L. V. E., Gavazzi R., Marshall P. J., Bolton A. S., 2010, ApJ, 709, 1195

Treu T., Koopmans L. V. E., 2004, ApJ, 611, 739

van de Ven G., De Zeeuw P. T., Van Den Bosch R. C. E., 2008, MNRAS, 385, 614

van den Bosch R. C. E., van de Ven G., Verolme E. K., Cappellari M., De Zeeuw P. T., 2008, MNRAS, 385, 647

van Dokkum P., Conroy C., Villaume A., Brodie J., Romanowsky A. J., 2017, ApJ, 841, 68

Vasiliev E., Valluri M., 2020, ApJ, 889, 39

Vaughan S. P., Davies R. L., Zieleniewski S., Houghton R. C. W., 2018, MNRAS, 475, 1073

Vazdekis A., Koleva M., Ricciardelli E., Röck B., Falcón-Barroso J., 2016, MNRAS, 463, 3409

Virtanen P. et al., 2020, Nature Meth., 17, 261

Wang Y. et al., 2019, MNRAS, 490, 5722

Weijmans A.-M. et al., 2014, MNRAS, 444, 3340

Wolf J., Martinez G. D., Bullock J. S., Kaplinghat M., Geha M., Muñoz R. R., Simon J. D., Avedo F. F., 2010, MNRAS, 406, 1220

Yang M., Zhu L., Weijmans A.-M., van de Ven G., Boardman N., Morganti R., Oosterloo T., 2020, MNRAS, 491, 4221

Zhu L. et al., 2018a, MNRAS, 473, 3000

Zhu L., van de Ven G., Méndez-Abreu J., Obreja A., 2018b, MNRAS, 479, 945

APPENDIX A: PROJECTED DENSITY MODELS

Table A1 presents both the stellar mass density and luminosity density MGE models for SNL-1. For the models in this work, the MGEs are assumed to be axisymmetric in projection, and so all components have the same position angle.

Table A1. MGE_Σ and MGE_μ for SNL-1. The columns represent, from left to right, the projected surface mass density, projected surface brightness, width (peak location), and axial ratio, respectively. By construction (Section 3.1), the Gaussians for both MGE models have the same widths and axis ratios. Moreover, all Gaussian components have the same fixed PA.

$\Sigma_\star$ ($M_\odot$ pc^{-2})	μ_B (L$_\odot$ pc^{-2})	σ (arcsec)	q
665 322.22	111 570.70	0.022	0.700
241 694.28	40 530.74	0.075	0.500
66 986.41	11 235.65	0.093	0.900
109 985.28	18 455.82	0.212	0.900
21 783.49	3657.34	0.491	0.900
43 580.97	7328.28	0.612	0.503
21 490.22	3619.68	1.279	0.500
6248.14	1053.47	1.396	0.812
3028.55	520.74	2.268	0.517
3128.43	551.26	3.426	0.740
712.15	135.44	8.168	0.846

APPENDIX B: SCHWARZSCHILD MODEL PARAMETER-SPACE EXPLORATION

Owing to the computationally expensive implementations of the Schwarzschild technique, sampling methods such as Marko Chain Monte Carlo are currently impractical for model selection. The exploration of the parameter-space is instead achieved with a grid search over reasonable parameter ranges. In the case of the q shape parameter, its maximum value is constrained by the flattening of the MGE model (van den Bosch et al. 2008). The search is initialized over a wide range in each parameter to avoid local minima, then follows the minimum χ^2 while iteratively decreasing the step size. The search terminates once all surrounding models produce worse fits to the data. The search over the parameter-space is shown in Fig. B1. This flexible grid approach still allows for the characterization of the parameter-space, in particular any degeneracies between parameters, despite its relative simplicity.

The goodness-of-fit metric used here is a re-normalized version of the χ^2. The normalization is a factor of $\sqrt{2 \times N_{obs} \times N_{GH}}$, where N_{obs} is the number of spatial bins, and N_{GH} is the number of kinematic moments fit by the model (four in this work; Section 2.2) – see Zhu et al. (2018a) for further discussion on the goodness of fit. In order to estimate the uncertainties of the model parameters (Table 2), we take all models within 1σ given by this normalized metric, and for each parameter compute the standard deviation marginalized over all other parameters.
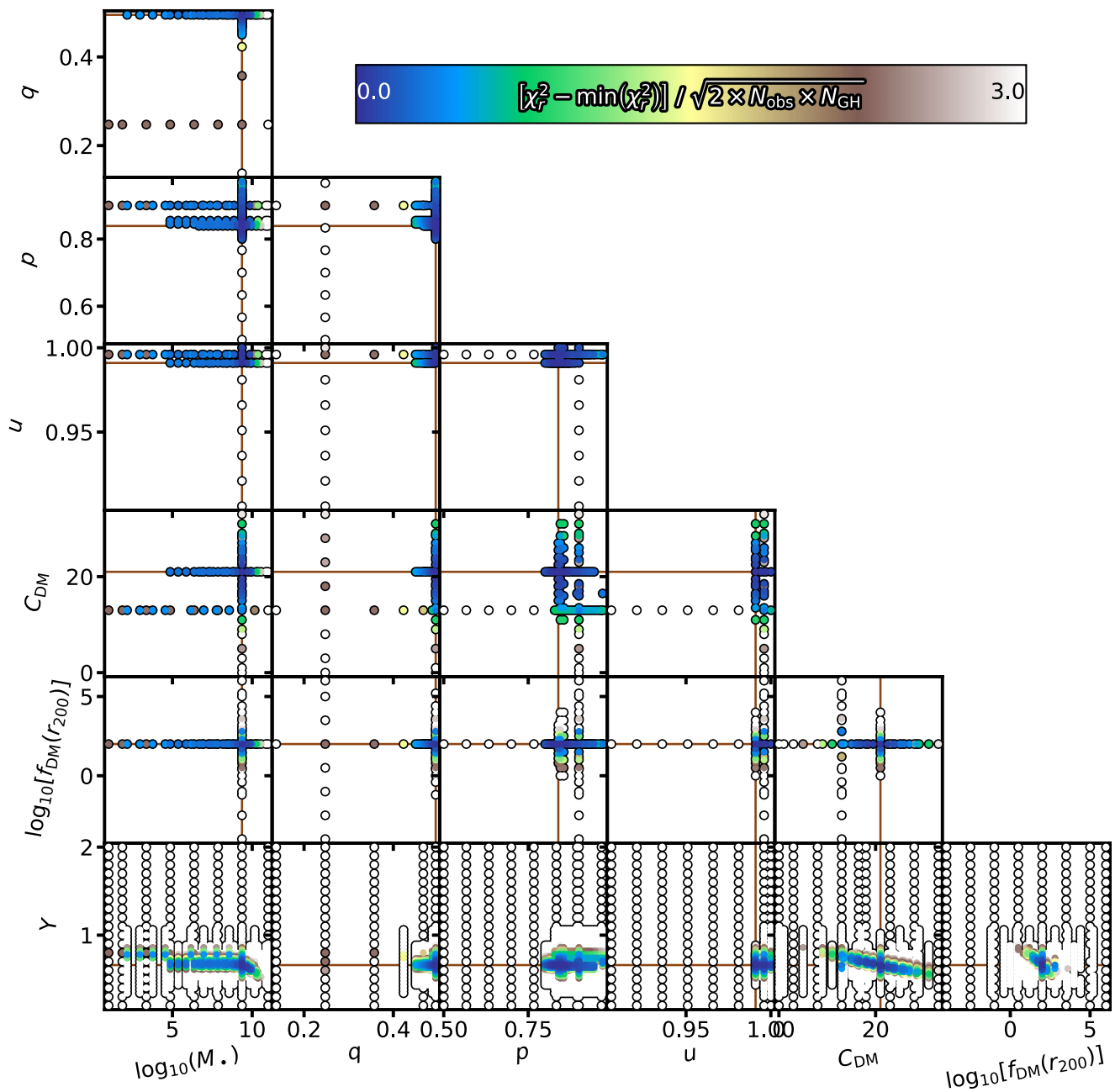
Figure B1. Schwarzschild model parameter-space, showing the exploration of all free parameters. Each model is shown as a point, coloured by its reduced χ^2. The best-fitting values are denote by the brown lines.

This paper has been typeset from a TEX/LATEX file prepared by the author.